

Electronic Supplementary Information

Solar water splitting exceeding 10% efficiency via low-cost Sb_2Se_3 photocathodes coupled with semitransparent perovskite photovoltaics

Wooseok Yang^{†a,b}, Jaemin Park^{†a}, Hyeok-Chan Kwon^{†a}, Oliver S. Hutter^c, Laurie J. Phillips^d, Juiwan Tan^a, Hyungsoo Lee^a, Junwoo Lee^a, S. David Tilley^b, Jonathan D. Major^d and Jooho Moon^{a*}

^a Department of Materials Science and Engineering, Yonsei University, 50 Yonsei-ro Sodaemun-gu, Seoul 03722, Republic of Korea

E-mail: jmoon@yonsei.ac.kr

^b Department of Chemistry, University of Zurich, Zurich 8057, Switzerland.

^c Department of Mathematics, Physics and Electrical Engineering, Northumbria University, Newcastle upon Tyne, UK.

^d Stephenson Institute for Renewable Energy, Physics Department, University of Liverpool, Liverpool L69 7ZF, UK

KEYWORDS:

Solar water splitting, Sb_2Se_3 photocathode, semitransparent photovoltaics, tandem, light management

Supplementary Figures

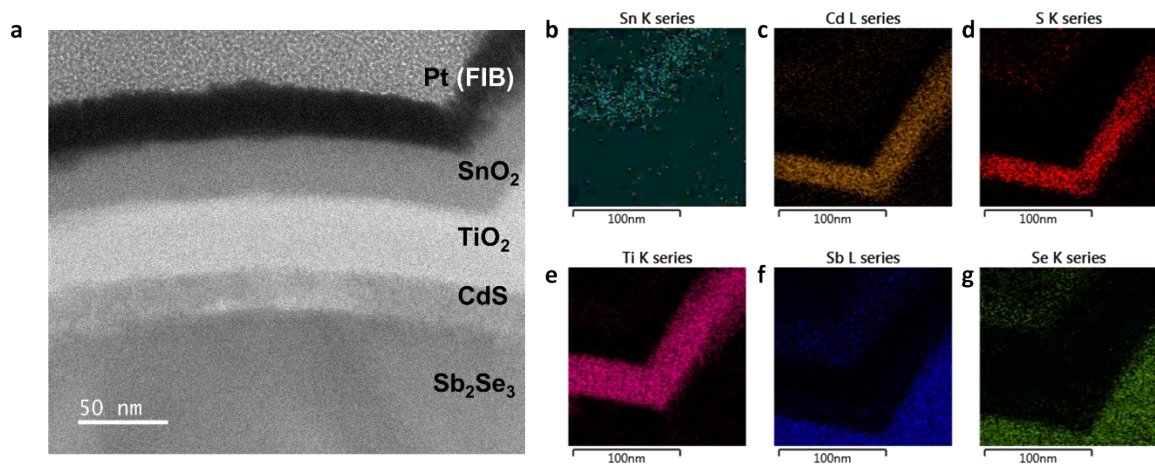


Fig S1. (a) Cross-sectional TEM image and (b-g) EDS mapping of SnO₂/TiO₂/CdS/Sb₂Se₃ junction.

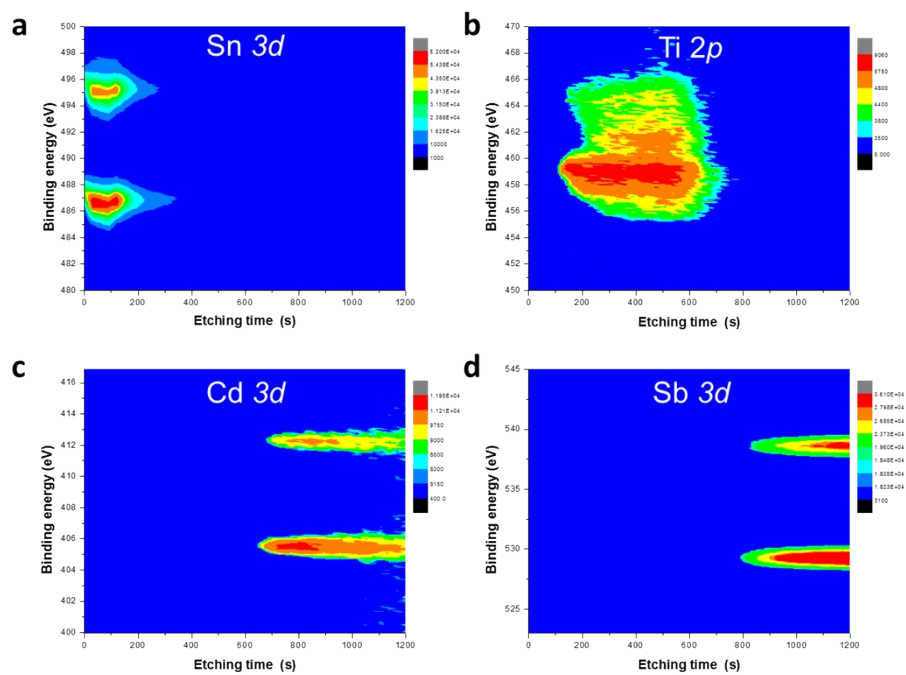


Fig S2. Elemental contour plots for the Sn, Ti, Cd, and Sb XPS signals.

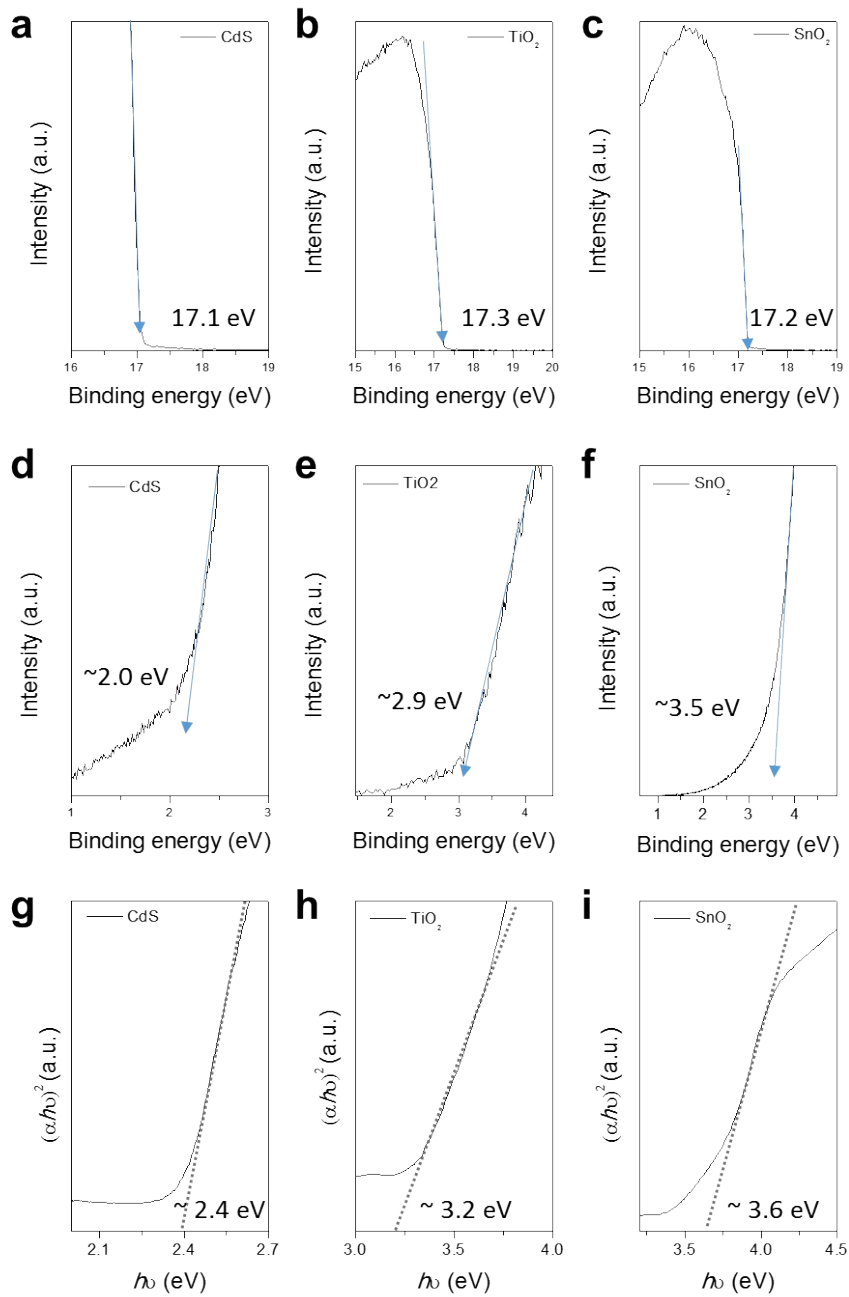


Fig S3. Ultraviolet photoelectron spectroscopy (UPS) measurement of (a-c) cutoff region and (d-f) valence band region. (g-i) Tauc plots obtained by UV-vis spectroscopy for band gap measurement of CdS (left), TiO₂ (middle), SnO₂ (right).

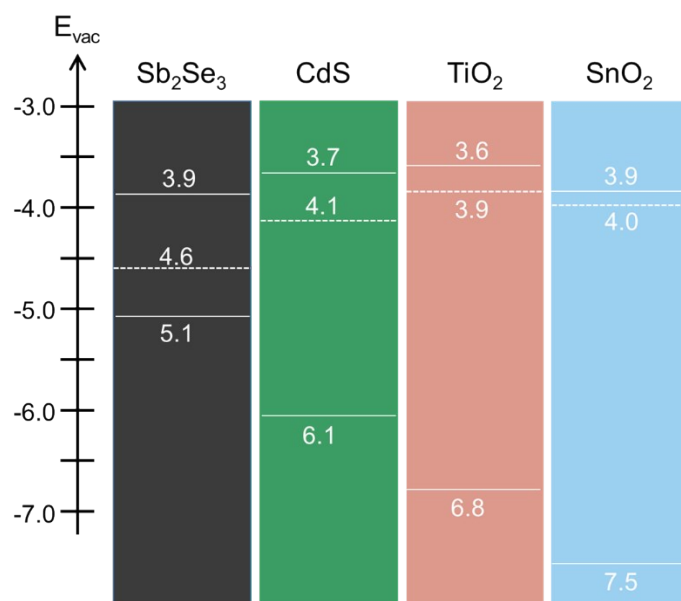


Fig S4. Non-equilibrium band alignment diagram of the Sb₂Se₃/CdS/TiO₂/SnO₂ heterojunction.

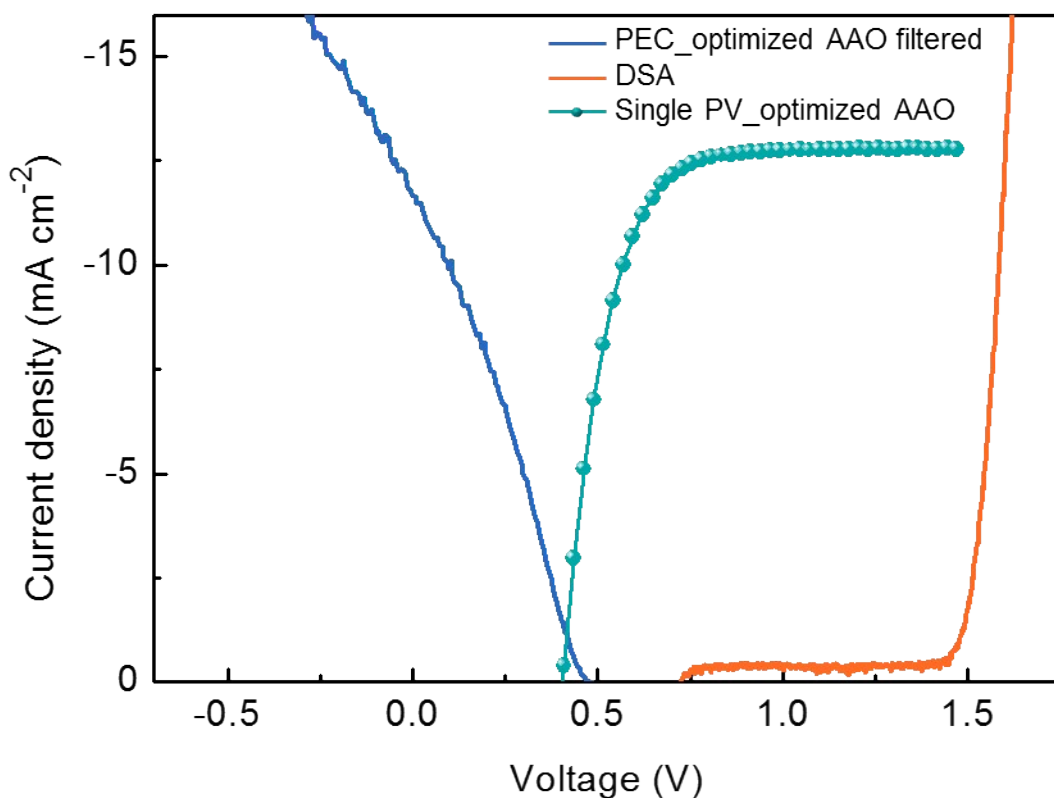


Fig S5. Single PV-cell-PEC tandem device. J–V curves of the semitransparent perovskite PV (single cell), DSA, and Sb₂Se₃ photocathode behind the PV. The current density at the operating point was approximately 1 mA cm⁻² (corresponding to $\eta_{\text{STH}} = 1.23\%$), indicating the necessity of using the PV module for a higher photovoltage.

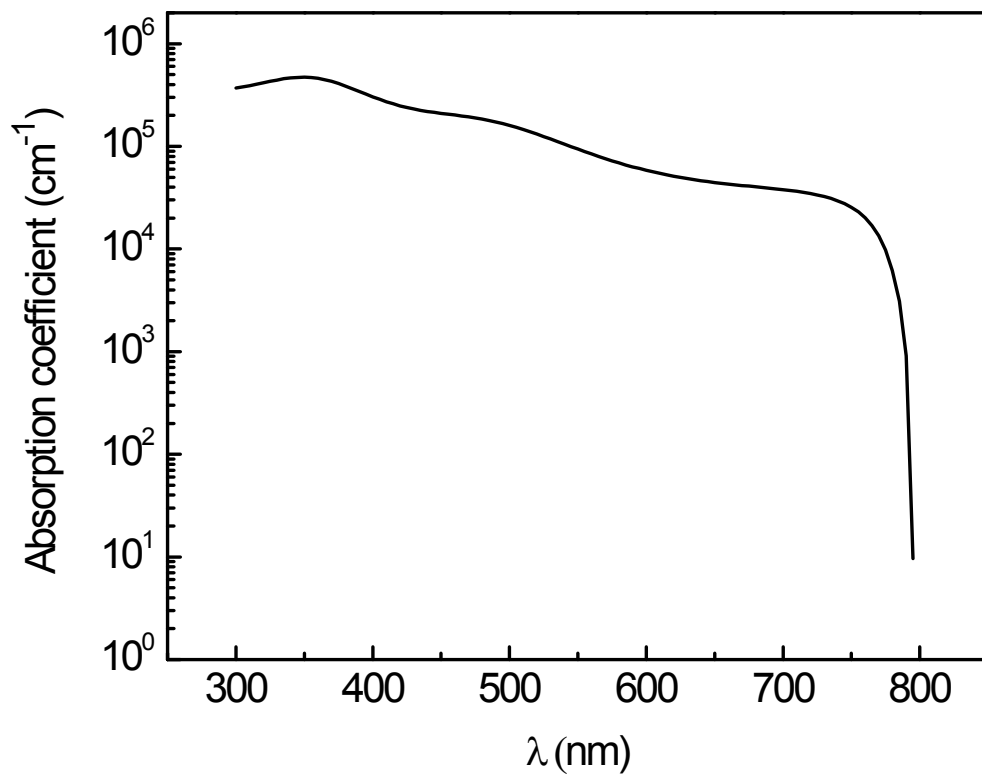


Fig S6. Light-absorption coefficient of MAPbI₃. The values are reported in literature (Ref. 26 in the main text), and the data can be accessed online (<https://www.pvlighthouse.com.au/refractive-index-library>).

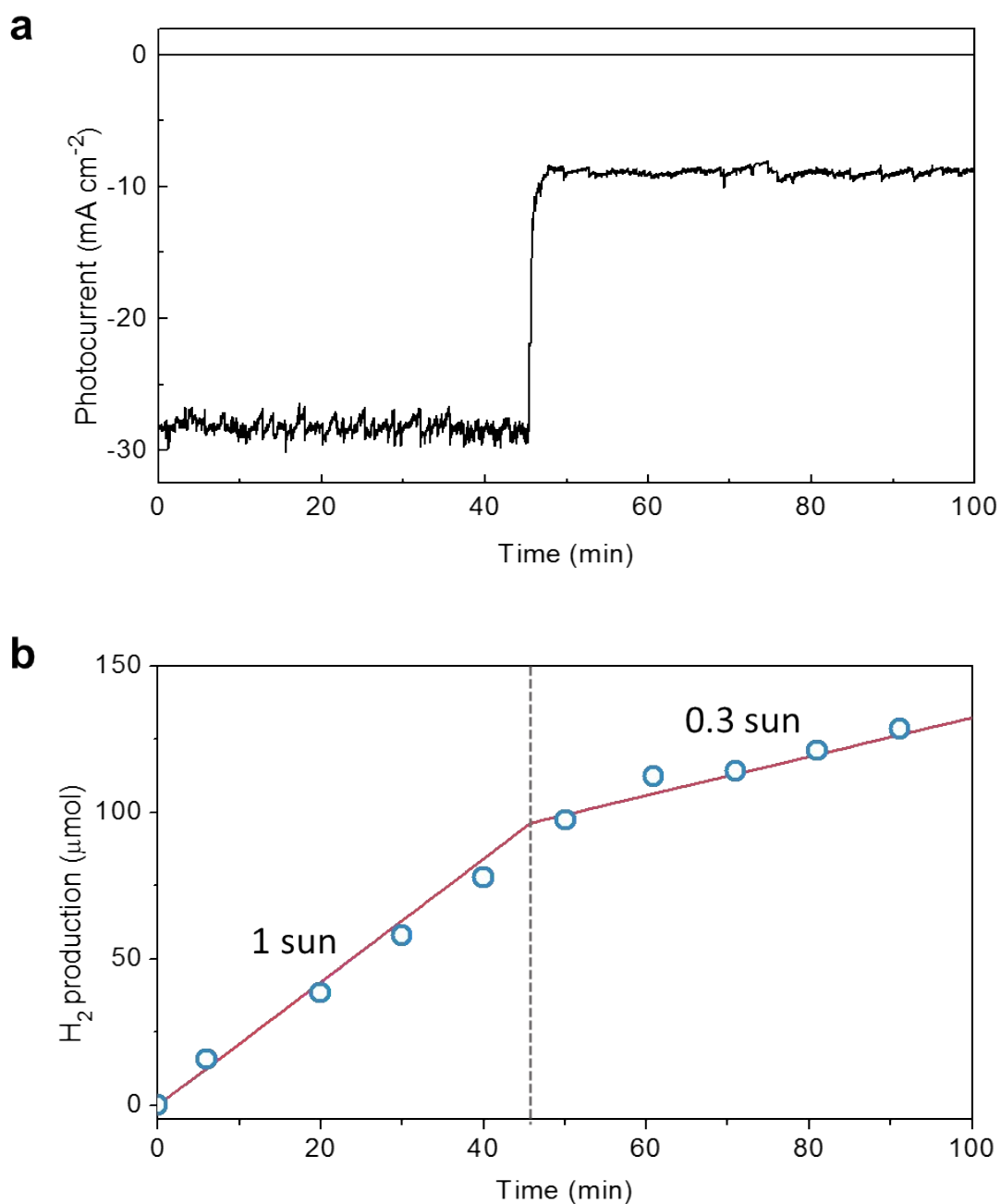


Fig S7. Faradaic efficiencies of the Sb₂Se₃ photocathodes. **a** Current density vs. time graph measured at 0 V_{RHE} under different light intensities and **b** corresponding time course curve of H₂ evolution. The solid line represents the time course curve for half of the electrons passing through the outer circuit ($e^-/2$). The dots indicate the amounts of H₂ gas, as measured by gas chromatography. The faradaic efficiency was close to 100% regardless of the current density.

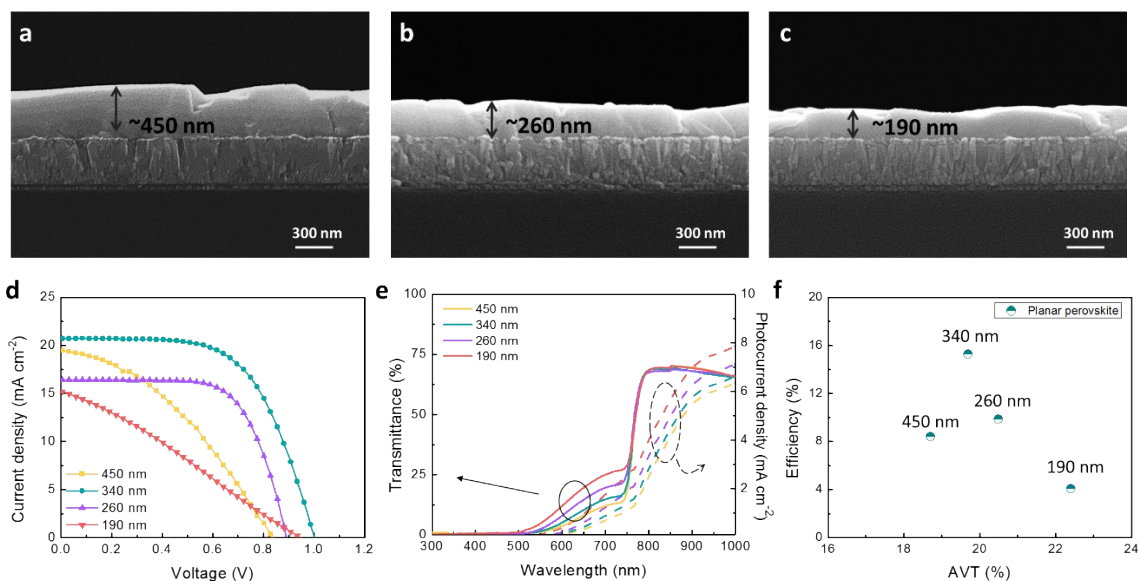


Fig S8. (a-c) Cross-sectional SEM images of planar perovskite thin films with different thickness. (d) J–V curves obtained by different thickness of perovskite with the FTO/TiO₂/perovskite/HTM/Au configuration, (e) transmittance of FTO/TiO₂/perovskite structures and the corresponding integrated photocurrent densities (dashed lines) of the Sb₂Se₃ photocathodes behind the planar PVs and (f) power conversion efficiencies of the planar PV cells with different thickness.

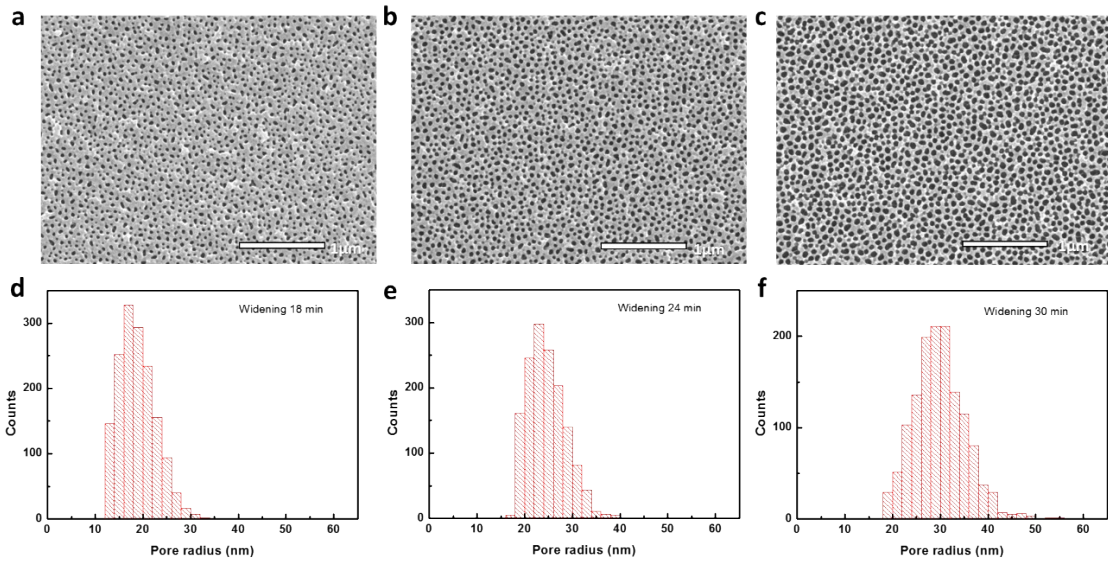


Fig S9. SEM images and pore size distribution of AAO templates with (a,d) 18 min, (b,e) 24 min, and (c,f) 30 min widening time.

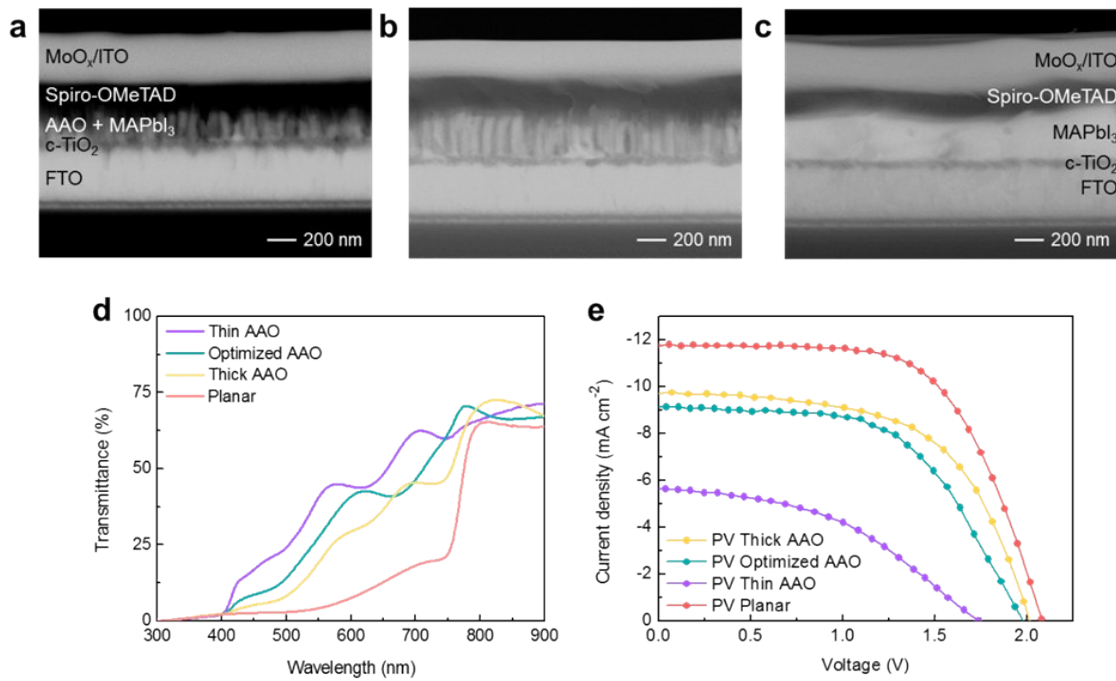


Fig S10. Cross-sectional SEM images of semitransparent perovskite PVs with (a) thin AAO template, (b) thick AAO template, and (c) planar perovskite thin film. (d) Total transmittance spectra and (e) J–V curves of the nanopillar and planar perovskite PVs.

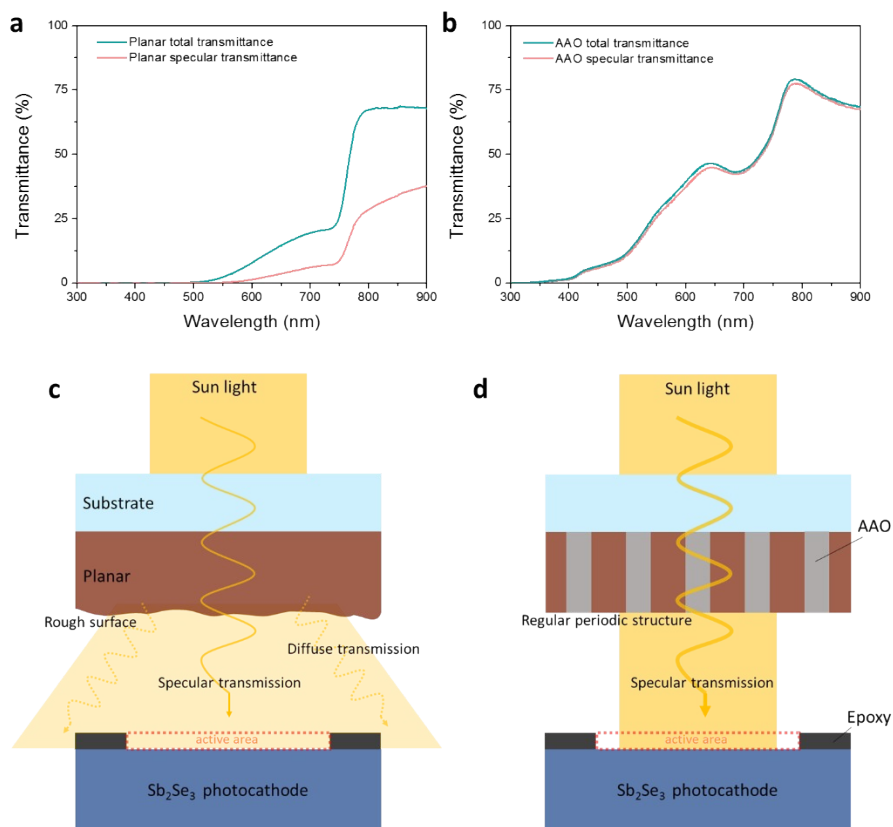


Fig S11. Total and specular transmittances of (a) planar and (b) AAO-perovskite layers on FTO/TiO₂ substrates. Schematics showing transmission through (c) planar and (d) AAO-perovskite layers.

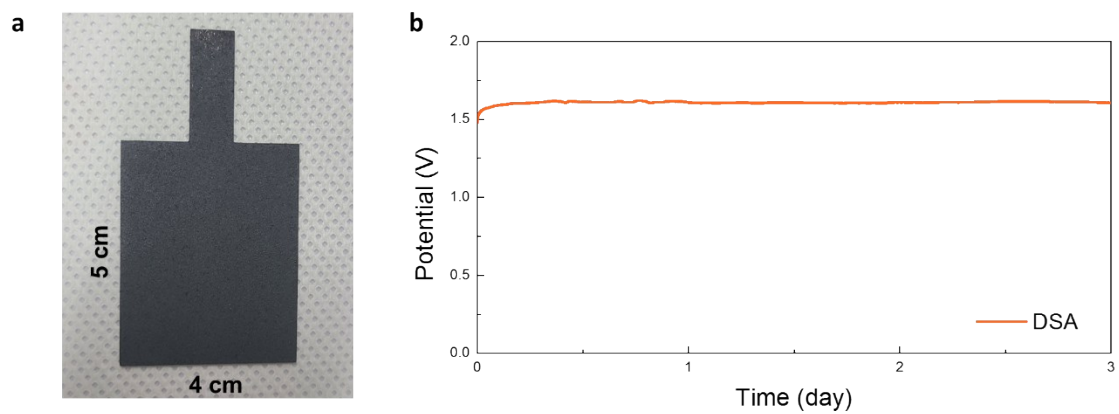


Fig S12. (a) Optical photograph and (b) a potential-time curve of DSA.

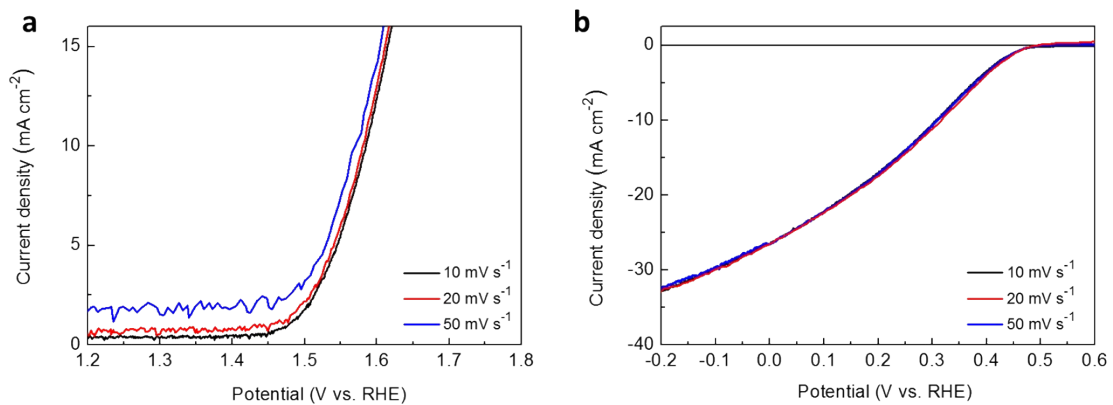


Fig S13. J–V curves of (a) DSA and (b) Sb₂Se₃ photocathodes with different scan speed.

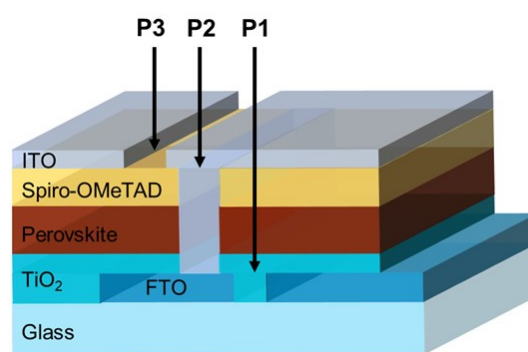


Fig. S14. Schematic showing two perovskite PV cells connected in series. For detailed experimental procedure, please refer to the experimental section in our previous study (*J. Mater. Chem. A*, **2020**, *8*, 1457–1468).

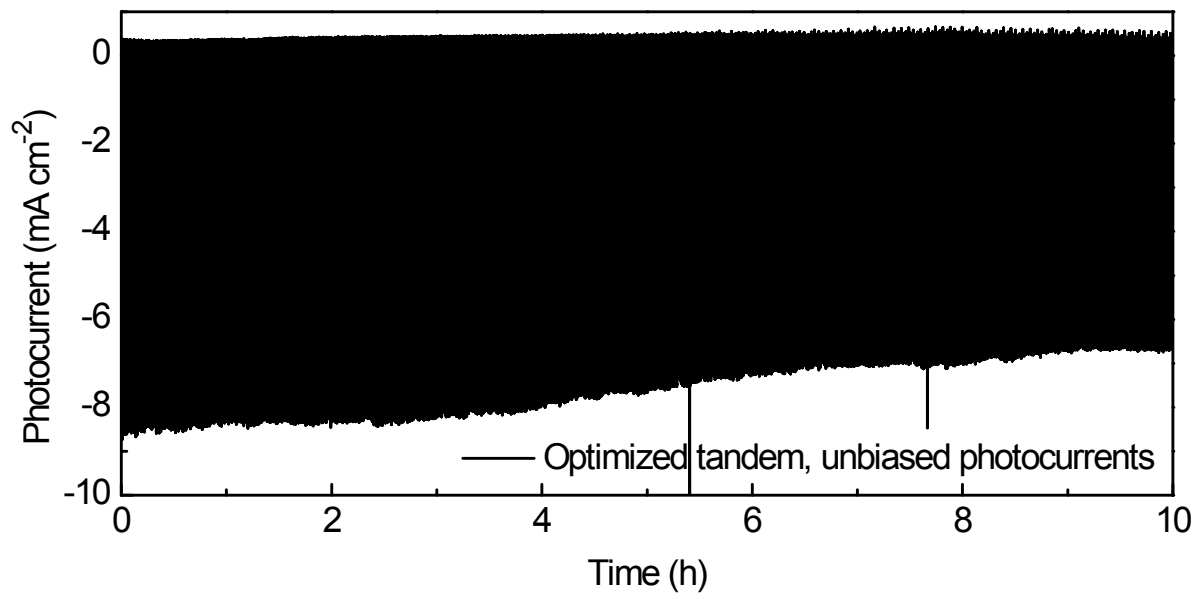


Fig S15. Long-term stability test of the optimized PV-PEC tandem cell.

Supplementary Table 1 | Performances of planar PVs with different perovskite thicknesses.

Thickness (nm)	AVT (300–900 nm)	V_{oc} (V)	J_{sc} (mA cm⁻²)	FF (%)	PCE (%)
~450	18.7	0.85	19.52	36.64	6.12
~340	19.7	1.01	20.71	60.44	12.64
~260	20.5	0.91	16.42	65.91	9.85
~190	22.4	0.95	15.23	28.10	4.06

Supplementary Table 2 | Performances of semitransparent PVs with different perovskite structures and thicknesses.

PV Type	Thickness (nm)	AVT (300–900 nm)	V_{oc} (V)	J_{sc} (mA cm⁻²)	FF (%)	PCE (%)
Planar	~340	19.7	2.08	11.75	62	15.26
Thick AAO	~290	31.1	2.08	9.70	57	10.93
Optimized AAO	~220	34.5	2.00	9.15	56	10.25
Thin AAO	~150	39.4	1.74	5.67	43	4.21

Supplementary Note 1

The series of energy-dispersive X-ray spectroscopy (EDS) elemental maps also show sharp edges in the spatial distribution of Sn, Ti, Cd, and Sb (Fig. S1b-g). In addition to EDS, which may not be reliable to detect representative interface properties over the sample, we have also performed X-ray photoelectron spectroscopy (XPS) depth profile measurements to further confirm the vertical distribution of the different layers in the junction. As the analysis area of the XPS measurement ($\sim 1 \text{ mm}^2$ spot) is larger than that of the TEM measurement ($\sim 100 \text{ nm}$), we could get more comprehensive information about the compositions with the XPS contour maps in Fig. S2. XPS data were collected after cycles of Ar^+ sputtering and only Sn was visible in the surface of the film, while Ti and Cd signals appeared after 150 s and 650 s of sputtering, respectively. This indicates the conformal coating of SnO_2 , TiO_2 , and CdS layers and no exposure of TiO_2 and CdS to the electrolyte. The Cd signal decreased with sputtering time but did not disappear completely. One possible explanation of the overlapping between the Cd and Sb signals is the inter-diffusion of CdS between Sb_2Se_3 , which is frequently reported in the literature.^{S1} Additionally, the roughness of the Sb_2Se_3 thin film higher than the thickness of the CdS layer ($\sim 20 \text{ nm}$) could be another possibility.

Supplementary Note 2

To provide experimental evidence for the band positions and band bending, UV-vis spectroscopy and ultraviolet photoelectron spectroscopy (UPS) have been performed as shown in Fig S3. The Fermi level position of each material can be obtained by subtracting the extrapolated values near the UPS cut off region from the He I source energy of 21.2 eV. For example, in the CdS case, the Fermi level is located at 4.1 eV ($21.2 \text{ eV} - 17.1 \text{ eV}$, Fig S3a) with respect to the vacuum level. The extrapolated values in the UPS valence band region represent the difference between the Fermi level and the valence band maximum (VBM) position. Therefore, in the CdS case, the VBM position is 6.1 eV ($4.1 \text{ eV} + 2 \text{ eV}$, Fig S3d). In addition, by subtracting the E_g values, obtained by the Tauc plot, from the VBM, the conduction band minimum (CBM) can be determined. In the CdS case, the CBM is located at 3.7 eV ($6.1 \text{ eV} - 2.4 \text{ eV}$, Fig S3g). All band positions and Fermi level positions were obtained in the same way. As a result, the band positions in non-equilibrium can be drawn as shown in Fig S4.

Supplementary Note 3

Seger et. al. showed that the electron tunneling in a TiO₂-electrolyte junction can even overcome a barrier more than 1 V (to drive the Fe(III) reduction near 0.77 V_{RHE} when the TiO₂ conduction band is pinned at -0.32 V_{RHE})^{S2}. They also estimated the tunneling probability (T_t) by using the Wentzel-Kramers-Brillouin (WKB) approximation as shown in Equation S1.

$$T_t = \exp \left[-\frac{4}{3} \Delta x \sqrt{\frac{2m_{eff}q\phi_b}{\left(\frac{h}{2\pi}\right)^2}} \right] \quad \text{Equation S1}$$

Here the tunneling probability increases exponentially as the square root of barrier height (Φ_b) decreases. Thus, although there is a small barrier (~ 0.1 V), the electron transfer from TiO₂ to SnO₂ is still highly probable in our case. Despite of the small barrier, therefore, the benefit of the SnO₂ layer in charge separation is clear. For more detailed calculations, interested readers can check reference S1.

Supplementary Note 4

Planar perovskite PV cells with different thickness were fabricated as shown in Fig. S8a-c. While the transmittance of the planar thin films increases with the decreasing thickness, the maximum efficiency of the planar PV cells is observed with the thickness of 340 nm (Fig. S8d-e). When the thickness is reduced from 340 nm to 190 nm, the average transmittance (AVT) slightly increases from 19.7 % to 22.4 %, which is potentially beneficial for a top electrode of tandem devices (Fig. S8f). In the meantime, however, the reduced film thickness results in a significantly detrimental effect on device performance (power conversion efficiency, η_{PCE} from 15.2 to 4.6 %) by losing photocurrent as well as the fill factor (Table S1). The dashed lines in Fig. S8e are the integrated photocurrent densities calculated based on the transmittance of the planar PV cells and the IPCE values of the Sb_2Se_3 photocathodes. The maximum photocurrent density achievable by the Sb_2Se_3 photocathodes behind the planar PV cells is below 8 mA cm^{-2} , indicating that the STH efficiency of the planar PV- Sb_2Se_3 photocathode cannot exceed 10 % even with an ideal case. The realistic STH efficiency of planar PV- Sb_2Se_3 tandem cells should be much lower as the most transparent planar PV (190 nm) has fairly low fill factors.

Supplementary Note 5

In the present study, the morphology of the AAO templates and the amount of perovskite were carefully optimized to maximize performance. The AAO templates were prepared by anodization of the Al thin film followed by a widening procedure in a phosphoric acid solution (see the experimental section for the details). The pore size of the AAO templates can be controlled by changing the dipping time. As shown in Fig. S9, the pore size increases with the widening time. The average pore radii are 20.5, 26.6, and 33.3 for 18, 24, 30 min widening time, respectively. As the pore size increased, the transmittance of the AAO-based perovskite cells decreased. In our previous study^{S3}, it was shown that the open-circuit voltage and the fill factor became low when the pore size was too small and the optimum transparency and performance can be achieved with 30 min for widening time. Thus, in the present study, we used 30 min for widening time and varied the filling level of the perovskite layers in the AAO scaffolds.

As we mentioned above, another important factor determining the transmittance and device performance of the AAO-templated perovskite cells is the filling level of the perovskite layer in the AAO scaffolds. We fabricated AAO-based perovskite cells with three different thicknesses (denoted as ‘thin’, ‘optimized’ and ‘thick’ in the manuscript) by changing the filling level. The filling level was determined by experimental conditions such as the concentration of the perovskite solution and the rpm for the spin coating process. For the ‘thin’ sample, 20 wt % solution with 4000 rpm coating speed was used, while other samples had different conditions (26 wt % with 4000 rpm for the ‘optimized’ sample, and 26 wt% with 1500 rpm for the ‘thick’ sample). The different filling amount made the differences in transmittance and performance. Figs. S10a and b show cross-sectional scanning electron microscopy (SEM) images of the semitransparent PVs with different AAO thicknesses. A normal planar thin film perovskite PV is shown in Fig. S10c. We used a spiro-OMeTAD/MoO_x/ITO layer as the transparent hole-selective contact in all the PV devices. With a thin AAO layer, the transmittance of the PV was high (Fig. S10d, dark violet line), which was beneficial for light absorption of the bottom electrode, but the overall η_{STH} was low owing to the low performance of the top PV (Fig. S10e, dark violet line). Supplementary Figs. 10d and e clearly indicate that the transparency and performance of the PV cells should be carefully optimized. The thickness, average visible light transmittance (AVT), open-circuit voltage (V_{OC}), short-circuit current

density (J_{SC}), fill factor (FF), and power-conversion efficiency (PCE) of each device are presented in Supplementary Table 2.

Supplementary references

S1 L. Wang, D-B. Li, K. Li, C. Chen, H-X. Deng, L. Gao, Y. Zhao, F. Jiang, L. Li, F. Huang, Y. He, H. Song, G. Niu, and J. Tang, *Nat. Energy*, 2017, **2**, 17046.

S2 B. Seger, S. D. Tilley, T. Pederson, P. C. K. Vesborg, O. Hansen, M. Grätzel and I. Chorkendorff, *J. Mater. Chem. A.*, 2013, **1**, 15089–15094.

S3 H. C. Kwon, S. Ma, S. -C. Yun, G. Jang, H. Yang and J. Moon, *J. Mater. Chem. A*, 2020, **8**, 1457–1468.